

# Journal of Materials Chemistry A

Accepted Manuscript



This is an *Accepted Manuscript*, which has been through the Royal Society of Chemistry peer review process and has been accepted for publication.

*Accepted Manuscripts* are published online shortly after acceptance, before technical editing, formatting and proof reading. Using this free service, authors can make their results available to the community, in citable form, before we publish the edited article. We will replace this *Accepted Manuscript* with the edited and formatted *Advance Article* as soon as it is available.

You can find more information about *Accepted Manuscripts* in the [Information for Authors](#).

Please note that technical editing may introduce minor changes to the text and/or graphics, which may alter content. The journal's standard [Terms & Conditions](#) and the [Ethical guidelines](#) still apply. In no event shall the Royal Society of Chemistry be held responsible for any errors or omissions in this *Accepted Manuscript* or any consequences arising from the use of any information it contains.

**An asymmetric supercapacitor with super-high energy density  
based on 3D core-shell structured NiCo-layered double  
hydroxide@carbon nanotube and activated polyaniline-derived  
carbon electrodes with commercial level mass loading**

Xiaocheng Li,<sup>a\*</sup> Juanjuan Shen,<sup>a,d</sup> Wei Sun<sup>a,c</sup>, Xuda Hong,<sup>b</sup> Rutao Wang,<sup>a</sup> Xinhong Zhao<sup>c</sup>, Xingbin

Yan<sup>a</sup>

<sup>a</sup>Laboratory of Clean Energy Chemistry and Materials, Lanzhou Institute of Chemical  
Physics, Chinese Academy of Sciences, Lanzhou 730000, P. R. China

<sup>b</sup>Shenzhen Institute of Advanced Technology, Chinese Academy of Sciences, 518055,  
P. R. China.

<sup>c</sup>School of Petrochemical Engineering, Lanzhou University of Technology, Lanzhou  
730050, P. R. China.

<sup>d</sup>Graduate University of Chinese Academy of Sciences, Beijing, 100080, P. R. China

**Abstract:** Realization of high cell energy density at high mass loading is a critical requirement for practical applications of supercapacitors. To date, the cell energy density of supercapacitor device is mainly limited by the low utilization efficiency of electroactive materials on positive electrode at high mass loading and the low capacitance value of common activated carbon material on negative electrode. In this study, a super-high energy density asymmetric supercapacitor device with commercial

---

\*Corresponding author. Tel./fax: +86-931-4968040; Email: xiaocheng@licp.cas.cn

mass loading was successfully fabricated by using 3D core-shell structured NiCo-layered double hydroxide@carbon nanotube (NiCo-LDH@CNT) composite as positive electrode and activated polyaniline-derived carbon (APDC) as negative electrode. Due to its unique core-shell structure, the NiCo-LDH@CNT/nickel foam (NF) electrode with a mass loading of  $8.5 \text{ mg/cm}^2$  delivered a high capacitance of  $2046 \text{ F g}^{-1}$  at  $1 \text{ A g}^{-1}$ , and still remained a high capacitance of  $1335 \text{ F g}^{-1}$  as current density increased up to  $15 \text{ A g}^{-1}$ . Coupled with high performance APDC-based negative electrode with a capacitance of  $487 \text{ F g}^{-1}$  at  $1 \text{ A g}^{-1}$ , the asymmetric NiCo-LDHs@CNT/NF//APDC/NF supercapacitor device delivered a maximum energy density of  $89.7 \text{ Wh kg}^{-1}$  with an operational voltage of  $1.75 \text{ V}$ , and a maximum power density of  $8.7 \text{ kW kg}^{-1}$  at an energy density of  $41.7 \text{ Wh kg}^{-1}$ , suggesting its promising applications in future.

**Keywords:** Nickel cobalt-layered double hydroxide; Core-shell; Carbon nanotube; Activated carbon; Polyaniline; Supercapacitor

## 1. Introduction

Among various power source devices, supercapacitors, offering higher power density than secondary batteries and higher energy density than conventional capacitors, are attracting much attention in recent few years.<sup>1,2</sup> Cobalt and/or nickel hydroxides are most studied positive electrode materials due to their highly reversible charge/discharge abilities, cost-effective and environmental-friendly nature. Recently,

NiCo-layered double hydroxide (NiCo-LDH) has been reported to be one of promising supercapacitive materials because it integrates the advantages of both two components and has superiority over either of single moieties in electrochemical process.<sup>3-8</sup> Inspired by the synergistic effect between nickel and cobalt elements, considerable efforts have been devoted to improving the electrochemical performance of NiCo-LDH by constructing different well-defined architectures, such as nanosheets,<sup>7, 9, 10</sup> nanoparticles,<sup>11, 12</sup> nanofilms,<sup>13</sup> nanorods,<sup>14</sup> nanowire,<sup>15</sup> and microspheres.<sup>6</sup> The developed NiCo-LDH nanostructures can deliver high specific capacitance and enhanced cycling stability due to their high specific surface area, reasonable mesoporous pore-size distribution and co-contribution of binary redox states resulted from Ni<sup>2+</sup>/Ni<sup>3+</sup> and Co<sup>2+</sup>/Co<sup>3+</sup> couples. Although great improvement was achieved, the practical application of NiCo-LDH still suffers from the poor rate capability due to its semiconductor nature.<sup>14, 16</sup> Even more challenging is that, similar as most metal oxides, the specific capacitance of NiCo-LDH is in contradiction to the mass loading of active material per area, which dramatically decreases with the increases of mass loading on current collector. In previous reports, the LDH-based electrodes demonstrating high specific capacitance of 1500-3000 F g<sup>-1</sup> usually have the low mass loading value of less than 3 mg/cm<sup>2</sup>,<sup>4, 5, 7, 15</sup> however, for the electrodes with mass loading value more than 5 mg/cm<sup>2</sup>, the specific capacitance is usually lower than 1000 F g<sup>-1</sup>.<sup>14, 17, 18</sup> To more precisely evaluate the performance of supercapacitive materials and meet the requirement of their practical applications, it has been recently suggested that electrode materials should be tested with commercial

mass loading (8-10 mg/cm<sup>2</sup>) on current collector.<sup>19,20</sup> In this case, how to efficiently utilize the supercapacitive materials with high mass loading is an on-going challenge. To address this problem, an efficient method is to grow the active materials on nano-architected current collectors and form a typical core-shell nanostructure.<sup>3, 5, 7, 14, 21, 22</sup> Among all various options for nano-sized current collectors, carbon nanotube (CNT) with excellent electronic conductivity, mechanical stability and high corrosion resistance, is an ideal candidate for deposition of active materials.<sup>23-27</sup> Therefore, construction of core-shell structured CNT@NiCo-LDH composite would be a good choice to resolve the big conflict between the mass loading and electrochemical performance of NiCo-LDH, and thus realize the high specific capacitance at high mass loading level.

Beside that of positive electrode, the electrochemical performance of negative electrode material is another key factor to determine the performance of supercapacitor device ( $C_{cell}$ ), as defined by the formula  $\frac{1}{C_{cell}} = \frac{1}{C_+} + \frac{1}{C_-}$ . Considering the fact that the capacitance of the metal oxide/hydroxide-based positive electrodes ( $C_+$ ) is several times higher than that of negative electrodes, the cell capacitance ( $C_{cell}$ ) of supercapacitor is decisively limited by the low capacitance value of negative electrode materials ( $C_-$ ). To meet the imminence demand for high performance negative electrode materials, several advanced carbonaceous architectures, such as activated carbon, CNT, graphene oxide, porous graphene and heteroatom (N, S, O, P)-doped carbon materials, are widely designed and prepared.<sup>24</sup> Among them, N-doped activated carbon materials are considered as most promising candidates due

to their extremely high capacitance resulted from the co-contribution of electrical double layer and faradic reactions. Moreover, the doping of nitrogen can remarkably improve the electrical conductivity of carbon hosts due to the higher electronegativity of nitrogen (3.5) than that of carbon (3.0),<sup>29</sup> which would promote the electron and/or ion transfer and thus boost the electrochemical performance of carbon materials.<sup>30</sup> Previously, the doping strategy is realized by exposing carbon materials in N-containing atmosphere (NH<sub>3</sub>) under high temperature or modifying the carbon materials with N-containing polymers, leading to a high cost or low doping efficiency.<sup>31</sup> Recently, direct carbonization of N-enriched precursors is regarded as an efficient method to produce N-doped carbon materials with high capacitance.<sup>3, 28, 32, 33</sup> By carbonization of commercial lower-vapor polymers (for example, polyaniline, PANI) followed by activation, it is possible to fabricate highly N-doped carbon materials with high active specific surface area, boosting the specific capacitance of negative electrode to be closer to that of the positive electrode.

With these two considerations in mind, in this study, we design and fabricate an advanced asymmetric supercapacitor (ASC) device by using 3D core-shell structured NiCo-LDH@CNT composite (NiCo-LDH: 8.5 mg/cm<sup>2</sup>) as positive electrode and activated polyaniline derived carbon (APDC) as negative electrode. Owing to the high electrochemical performances of positive and negative electrodes, the ASC device exhibits a high cell capacitance of 210.9 F g<sup>-1</sup> and a maximum energy density of 89.7 Wh kg<sup>-1</sup> at a power density of 456.8 W kg<sup>-1</sup>. Furthermore, two such 1 cm<sup>2</sup> ASC device connected in series can efficiently power a commercial red LED indicator for 10 min

and robustly drive a 3V minifan for 4 min after charging by an AA battery for only 10 s, demonstrating its promising commercial applications in future.

## 2. Experimental details

### 2.1 Fabrication of NiCo-LDH/CNT/NF positive electrode.

NFs (10 mm×10 mm×1.6 mm, 110 PPI,  $420\pm 25\text{ g m}^{-2}$ , Changsha Lyrun Material Co., Ltd. China) sequentially cleaned with diluted hydrochloric acid, acetone and deionized water were used as substrates for CNT growth. The growth of CNT layer was performed via a thermal chemical vapor deposition (TCVD) process by using NF itself as catalyst, as described elsewhere.<sup>34</sup> Prior to growth of CNTs, the cleaned NF substrates were put into the centre of a quartz tube furnace and purged by Ar gas to remove the residual air. Then the furnace was heated up to 600 °C with a ramp rate of 10 °C/min and annealed for 5 min under H<sub>2</sub> atmosphere pressure with a flow rate of 50 sccm. After growing CNTs for 20 min with C<sub>2</sub>H<sub>2</sub> as carbon source (10 sccm), the samples were naturally cooled down to room temperature under H<sub>2</sub> atmosphere and taken out from furnace for depositing electroactive materials. The deposition of NiCo-LDH was performed using a commercial CHI660E electrochemical workstation (Chenhua Instrument Co., China) in a standard three-electrode cell configuration at a cathodic potential of -0.7 V within a mixed electrolyte solution containing 0.1 M Ni(NO<sub>3</sub>)<sub>2</sub>, 0.2 M Co(NO<sub>3</sub>)<sub>2</sub> and 0.075 M NaNO<sub>3</sub>. After electrodeposition, the samples were rinsed with copious deionized water for several times followed by drying at 80 °C for 2 h.

### 2.2 Synthesis of APDC nanorod negative electrode.

Synthesis of APDC was realized by carbonization of PANI precursor followed by a KOH activation process. The PANI precursor was synthesized via an oxidative polymerization route, as described in detail elsewhere.<sup>35</sup> After preparation, the resulting PANI precursor was pyrolyzed at 800 °C for 1 h under Ar atmosphere to obtain PANI-derived carbon (PDC). The activation process was performed by impregnating PDC powder with KOH (PDC: KOH = 1:6, wt%) in aqueous solution and then heated at 80 °C to remove residual water followed by heating at 700 °C for 1h under Ar atmosphere. After being cooling down to room temperature, the resulting product was neutralized by 5% HCl solution followed by repeatedly washing with copious deionized water, and finally dried at 60 °C in air for characterization.

### 2.3 Structural characterization

The as-prepared samples were characterized by an X-ray diffractometer (XRD, D/max-2400, Rigaku, Japan) with radiation from a Cu target ( $K\alpha$ ,  $\lambda=0.1541$  nm), a field-emission electron microscopy (FESEM; JSM-6701, JOEL), a high resolution transmission electron microscopy (HRTEM; JEM 2010F, JOEL) and an X-ray photoelectron spectroscopy (XPS, Perkin-Elmer PHI-5702) with 1486.6 eV radiation as excitation source.

### 2.4 Electrode preparation and electrochemical measurements

The NiCo-LDH/CNT/NF samples were directly used as positive electrode without further treatment. The negative electrodes were prepared by adding 5% of poly(tetrafluoroethylene) into the mixed powder of APDC (80wt%), acetylene black

(7.5wt%), conducting graphite (7.5wt%) and grinding for several minutes followed by spreading the resulting slurry on NFs. The electrodes were dried in air for 2h, pressed at 5 MPa, and further dried at 80 °C for 12 h.

Electrochemical performances of all as-prepared electrodes were firstly evaluated by electrochemical workstation within a three-electrode cell configuration containing 1 M KOH aqueous solution. The capacitances of all electrodes were calculated based on equation as follows:

$$C_s = I * \Delta t / (\Delta V * m) \quad (1)$$

where  $C_s$  (F g<sup>-1</sup>) is specific capacitance,  $I$  (A) is discharge current,  $\Delta t$  (s) is discharge time,  $\Delta V$  (V) is the window potential during the discharge, and  $m$  (g) is the mass of active materials (NiCo-LDH or APDC) on current collector. Electrochemical impedance spectroscopy (EIS) measurements were carried out at 0.24 V in an alternating current frequency ranging from 0.01 to  $3 \times 10^4$  Hz with an excitation signal of 5 mV.

For cell performance evaluation, an ASC device was assembled by using as-prepared NiCo-LDH@CNT/NF as positive electrode, APDC as negative electrode, commercial cellulose paper as separator and 1M KOH solution as electrolyte. To balance the charges stored on two electrodes ( $q^+ = q^-$ ), the mass loading ratio of electroactive materials on two electrode was obtained by the equation as follow:

$$\frac{m_+}{m_-} = \frac{C_- \times \Delta E_-}{C_+ \times \Delta E_+} \quad (2)$$

where  $m$ ,  $C$  and  $\Delta E$  are mass of active material, capacitance and potential window of the electrode, respectively; “+” and “-” represent positive and negative electrode, respectively. The capacitance of the assembled ASC device was calculated from eqn (1) based on the total mass of active materials (NiCo-LDH and APDC) on both two electrodes. The energy density and power density were calculated from following two equations:

$$E = \frac{C \cdot \Delta V^2}{7.2} \quad (3)$$

$$P = E \times 3600/t \quad (4)$$

where  $E$  (Wh kg<sup>-1</sup>) and  $P$  (W kg<sup>-1</sup>) are energy density and power density, respectively. The definitions of  $C$ ,  $\Delta V$  and  $t$  are the same as those in eqn (1).

### 3. Results and Discussion

#### 3.1 Fabrication and characterization of NiCo-LDH@CNT/NF positive electrode

In present study, CNTs were used as core material to support electroactive NiCo-LDH and construct core-shell structured composite electrode. After TCVD process, the color of NF surface changes from intrinsic metallic gloss to dark black. FESEM image, as shown in Fig. 1a, indicated that a black dense hairy layer was uniformly distributed on skeleton of 3D cross-linked NF surface. High-magnification FESEM image (Fig. 1b) and Raman spectrum (Fig. S1) clearly demonstrated that this dense hairy CNT layer with thickness of ~5 μm was virtually composed of randomly entangled CNTs with diameter ranging from 20-250 nm and length up to ~10 μm, forming a self-supported 3D porous conductive nanostructure. By weighing the NF

substrate before and after TCVD process, the weight density of CNTs on NF is calculated to be  $\sim 16 \text{ mg/cm}^2$ . The growth of CNTs on NF is actually an in-situ self-catalyzed CVD process, which enables the formation of  $\text{sp}^2\text{-C-Ni}$  covalent bond and leads to a strong interfacial adhesion between CNTs and NF substrate (Fig. S2). Combined with the high intrinsic electrical conductivity, strong interfacial adhesion and large specific surface area, the integrated CNT/NF composite substrate can serve as a reliable binder-free current collector and simultaneously act as a good template to synthesize 3D hierarchical core-shell structured NiCo-LDH@CNT composite for supercapacitor applications.

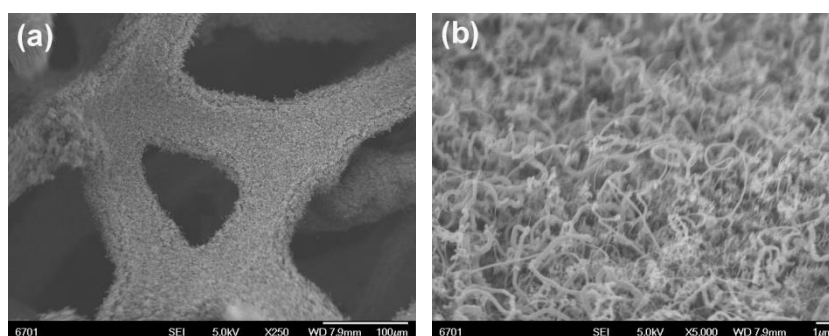


Fig. 1 Low magnification (a) and high magnification (b) FESEM images of CNT layer on NF substrate.

The deposition of NiCo-LDH was performed within a three-electrode cell configuration. The ratio of Ni/Co has significant effect on the electrochemical performance of resulting NiCo-LDHs. According to previous reports, NiCo-LDH with Ni/Co ratio of 1:2 presented the best supercapacitive performance among all NiCo-LDHs.<sup>7, 8, 14, 36</sup> Therefore, the complex metal nitrate precursors with Ni/Co ratio of 1:2 were used as electrolyte for depositing NiCo-LDH in present study. After

electrochemical deposition, the color of the sample surface changed from dark black to light green color, indicating the successful deposition of metal hydroxides. XRD patterns, as shown in Fig. S3, indicated the formation of crystallized NiCo-LDH with mixed phases of  $\alpha$ ,  $\beta$ -Ni(OH)<sub>2</sub> and  $\alpha$ ,  $\beta$ -Co(OH)<sub>2</sub>. EDS spectrum (Fig. S4) confirmed that the Ni/Co ratio in NiCo-LDH was roughly equal to 1:2, which is consistent with that in precursor solution due to the approximately equal solubility product constant ( $K_{sp}$ ) of Ni(OH)<sub>2</sub> and Co(OH)<sub>2</sub>.<sup>34</sup> Fig. 2a-c shows FESEM images of the as-prepared NiCo-LDH@CNT/NF composite electrode. It can be observed that, after electrodeposition, NiCo-LDH nanoflakes were uniformly deposited on CNT skeleton and formed a well-defined individual distribution of NiCo-LDH@CNT core-shell nanostructure (Fig. 2a and b). No aggregation of NiCo-LDH nanoparticles off CNT support were observed, implying that the nucleation and deposition of NiCo-LDH only occurred on the exterior surfaces of CNTs. From high magnification FESEM (Fig. 2c), it was found that the CNT core layer was totally surrounded by vertically-aligned NiCo-LDH nanoflakes with thickness of ~27 nm, closing to the maximum depth of ~20 nm for electroactive materials to participate the pseudocapacitive reactions. The open space between neighboring nanoflakes and neighboring NiCo-LDH@CNT core-shell nanostructures allows an easy access of ions to the electrolyte/electrode interface and facilitates the occurrence of faradic reactions during energy conversion process. In contrast, the NiCo-LDH directly deposited on NF substrate showed a rather compact distribution of nanoflakes, leading to a much reduced specific surface area (Fig. S5 and Fig. 3c). HRTEM image as

shown in Fig. 2d demonstrated that NiCo-LDH nanoflakes still tightly anchored on the sidewall of CNTs even after ultrasonic treatment during TEM sample preparation, further confirming the strong interfacial adhesion between CNTs and NiCo-LDH. Selected area electron diffraction (SAED) pattern taken from nanoflakes on sidewall of MWCNTs displayed as two well-defined diffraction rings, suggesting the polycrystalline characteristics of NiCo-LDH, which is in good agreement with the XRD results in Fig. S3. All above observations confirm the successful preparation of 3D hierarchical NiCo-LDH@CNT core-shell structure on macroporous NF substrate and pave the way for its electrochemical performance investigation.

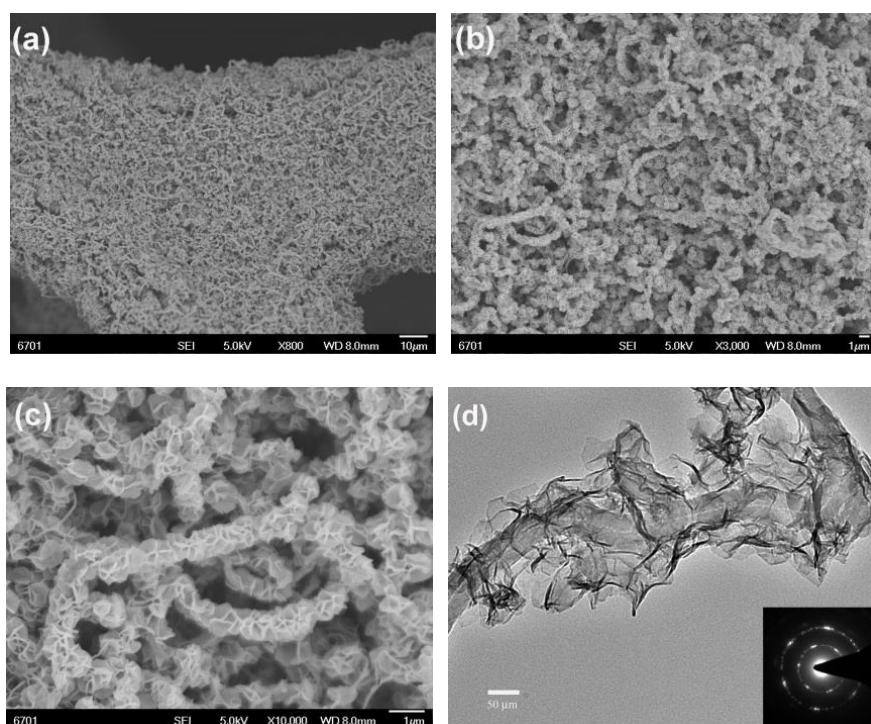


Fig. 2 (a) Over-view, (b-c) high magnification FESEM images NiCo-LDH@CNT electrode and (d) HRTEM image of NiCo-LDH@CNT core-shell structure. Inset in Fig 2(d) is corresponding SAED pattern taken from NiCo-LDH nanoflakes.

Figure 3a presents the CV curves of the as-prepared NiCo-LDH@CNT/NF

electrode with mass loading of  $8.5 \text{ mg/cm}^2$  at scan rates ranging from  $1\text{-}10 \text{ mV s}^{-1}$ . Unlike the rectangular shaped CV curve of EDLC-based electrodes, all CV curves of NiCo-LDH@CNT/NF electrode at various sweep rates demonstrated typical pseudocapacitive characteristic with a couple of highly reversible redox peaks within a potential window of  $-0.4\text{-}0.6 \text{ V}$ , which is attributed to the faradic redox reactions between M-OH and M-O-OH (where the M represents the Ni or Co ions). It should be noted that the capacitance contribution of CNT/NF substrate to NiCo-LDH@CNT/NF electrode is extremely low and can be neglected. This can be verified by its linear CV shape along potential-axis as compared to that of NiCo-LDH@CNT/NF electrode with large integral area (Fig. S6a-c).

Fig. 3b demonstrates the discharge curves of the NiCo-LDH@CNT/NF within a potential range of  $-0.1\text{-}0.4 \text{ V}$  at various current densities. The corresponding specific capacitances were calculated based on eqn (1) and are plotted in Fig. 3c. Encouragingly, the NiCo-LDH@CNT/NF electrode with mass loading of  $8.5 \text{ mg/cm}^2$  can deliver the high capacitances of 2046, 1938, 1923, 1680 and  $1335 \text{ F g}^{-1}$  at 1, 3, 5, 10 and  $15 \text{ A g}^{-1}$ , respectively, suggesting the excellent capacitive performance at high mass loading level. In contrast, for NiCo-LDH/NF electrode, although the comparable specific capacitance values can be achieved at low mass loading level ( $0.54 \text{ mg/cm}^2$ ), disappointingly, they dramatically reduced to 762, 489, 376 and  $258 \text{ F g}^{-1}$  at current densities of 1, 3, 5 and  $10 \text{ A g}^{-1}$ , respectively, as mass loading increased up to  $2.29 \text{ mg/cm}^2$  (blue curve in Fig. 3c). This implies that the utilization efficiency of NiCo-LDH on CNT/NF is much higher than that on NF, which can be further verified

by the normalized CV curves (per unit gram) of two electrodes at a sweep rate of  $5 \text{ mV s}^{-1}$  (Fig. 3d). All these clearly demonstrate the significant role of CNT/NF composite current collector in improving the specific capacitance, rate capability of NiCo-LDH. To bet of our knowledge, the electrochemical performance of NiCo-LDH/CNT/NF electrode is also competitive with those of LDHs in previous reports as listed in Table 1.

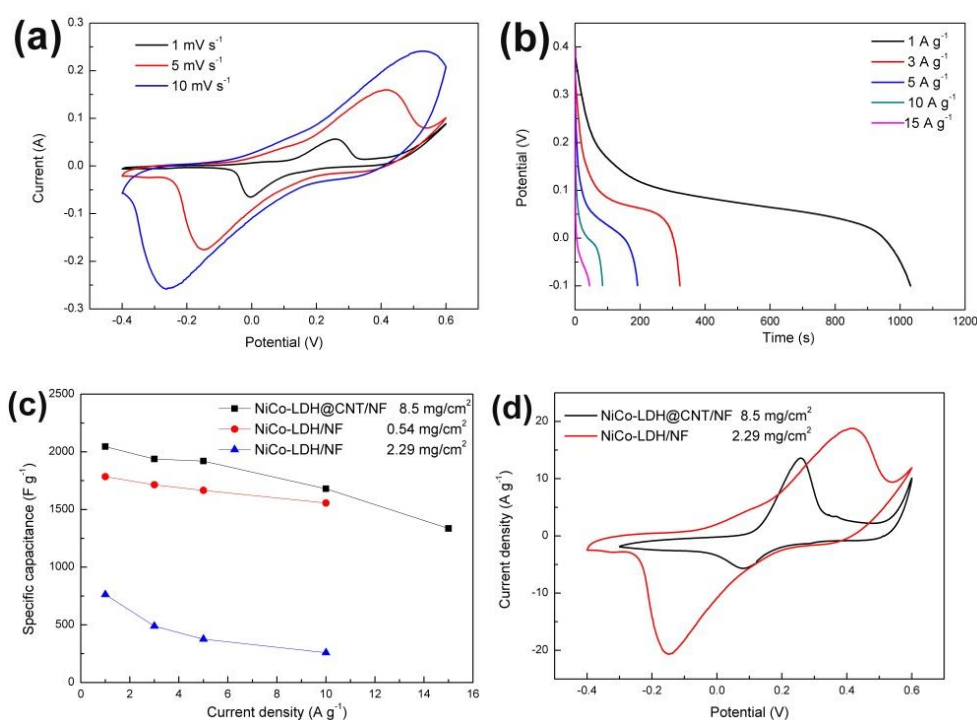


Fig. 3 Electrochemical performances of NiCo-LDH@CNT/NF and NiCo-LDH/NF electrodes: (a) CV curves at various scan rates and (b) discharge curves at various current densities of NiCo-LDH@CNT/NF electrode, (c) Specific capacitance comparison of two electrodes at different mass loadings, and (d) Normalized CV curves (per unit gram) of two electrodes at a scan rate of  $5 \text{ mV s}^{-1}$ .

Table 1 Comparison of the electrochemical performance of NiCo-LDH@CNT/NF electrode with

those in previous reports.

Electrode structure	$C_s$ (F g <sup>-1</sup> )	Rate capability	Mass loading	Ref.
NiAl-LDH-30G/NF	1255.8 (1 A g <sup>-1</sup> )	755.6 (6 A g <sup>-1</sup> )	5 mg/cm <sup>2</sup>	18
NiCo-LDH/NF	804 (3 A g <sup>-1</sup> )	500 (15 A g <sup>-1</sup> ) <sup>a</sup>	2.8 mg/cm <sup>2</sup>	14
NiCo-LDH/Zn <sub>2</sub> SnO <sub>4</sub> /SS	1805 (0.5 A g <sup>-1</sup> )	1275 (100 A g <sup>-1</sup> )	0.25 mg/cm <sup>2</sup>	5
NiAl-LDH/NF	701 (10 mA cm <sup>-2</sup> )	164 (100 mA cm <sup>-2</sup> )	20 mg/cm <sup>2</sup>	17
NiCo-LDH/CNT/SS	502 (5 mV s <sup>-1</sup> )	276 (100 mV s <sup>-1</sup> )	0.75 mg/cm <sup>2</sup>	37
NiCo-LDH/NF	2104 (1 A g <sup>-1</sup> )	---	~10 mg/cm <sup>2</sup>	36
CoAl-LDH/GNS/NF	711 (1 A g <sup>-1</sup> )	516 (10 A g <sup>-1</sup> )	~5 mg/cm <sup>2</sup>	38
NiCo-LDH@CNT/NF	2046 (1 A g <sup>-1</sup> )	1335 (15 A g <sup>-1</sup> )	8.5 mg/cm <sup>2</sup>	This work

<sup>a</sup> Estimated from the published graph. SS and G represent for stained steel and graphene, respectively.

To explore the nature of performance difference of NiCo-LDH@CNT/NF electrode and NiCo-LDH/NF electrode, we perform the impedance measurement of two electrodes. As shown in Fig. 4, both of two EIS spectra revealed a partial semi-circle in high-/media frequency region relating to faradic charge transfer resistance and a nearly straight line along imaginary axis at low frequency region relating to mass diffusion process. For EIS spectrum of NiCo-LDH@CNT/NF electrode, the diameter of semi-circle is much smaller than that NiCo-LDH/NF electrode, indicating a lower charge transfer resistance at electrolyte/electrode interface. The slope of the straight line of NiCo-LDH@CNT/NF electrode at low frequency region is also much stiffer than that of NiCo-LDH/NF electrode, implying a lower mass diffusion resistance from electrolyte to electrode. Therefore, the superior electrochemical performance of NiCo-LDH@CNT/NF electrode can be accounted from by considering the following respects: 1) the 3D hierarchical CNT/NF composite current collector enables the

deposition of NiCo-LDH nanoflakes with large specific surface area and thus improves the utilization efficiency of NiCo-LDH; 2) the big open space between neighboring NiCo-LDH@CNT core-shell structures and neighboring NiCo-LDH nanoflakes facilitates the access of ions to electrode surface and thus shortens the ion diffusion path; 3) the typical core-shell structured NiCo-LDH@CNT greatly shortens the electron transport distance and reduce the charge transfer resistance, leading to a significant improvement of the rate capability of NiCo-LDH material; 4) the good interfacial contact between nanoflakes, CNT scaffold and NF substrate greatly lower the internal resistance of NiCo-LDH@CNT/NF electrode.

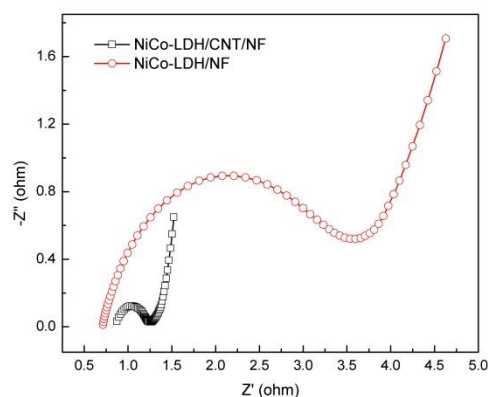


Fig. 4 EIS spectra of NiCo-LDH@CNT/NF and NiCo-LDH/NF electrodes.

### 3.2 Morphology and electrochemical properties of APDC-based negative electrode

Figure 5a-c shows the surface morphology of the as-prepared APDC powder. As demonstrated, the as-prepared APDC powder was actually composed of nanorods with diameter of  $\sim 100$  nm (Fig. 5a and b). Higher magnification HRTEM image suggest that the nanorod has a typical mesoporous characteristic with graphitic carbon at edge (Fig. 5c and inset). The survey scan XPS spectrum (panel A of Fig. 6)

confirmed the presence of nitrogen in APDC nanorods with content of 2.4wt%. The emission spectra of N1s (panel B of Fig. 6b) can be fitted into four component peaks representing pyridinic N (N-6, 398.6 eV), pyrrolic/pyridonic N (N-5 at 400.3 eV), quaternary N (N-Q at 401.3 eV) and oxidized N (N-X at 402.5 eV) with percentages of 12.8%, 53.4%, 25.5% and 8.5%, respectively. Previous reports suggest that N-Q group can greatly improve the electrical conductivity of carbon materials. The N-5 and N-6 groups can effectively take part in pseudocapacitive reaction and thus enhance the electrochemical performance of carbon materials.<sup>39-41</sup> As shown in Fig. 7a, CV loops at various sweep rates exhibited a quasi-rectangular shaped curves coupled with a prominent broad faradic redox hump. The former is essentially derived from the contribution of EDLC formed on carbon/electrolyte interface, while the latter is mainly resulted from the N-containing groups, especially from N-5 and N-6 groups. Thanks to the co-contribution of EDLC and faradic reactions, the as-prepared APDC-based electrode delivered high capacitances of 487, 392, 350, 305, 246 and 187 F g<sup>-1</sup> at current densities of 1, 2, 3, 5, 10 and 20 A g<sup>-1</sup> (Fig. 7b and inset), suggesting the excellent capacitive performance and making it as an ideal negative electrode material to match with NiCo-LDH-based positive electrode for supercapacitor applications.

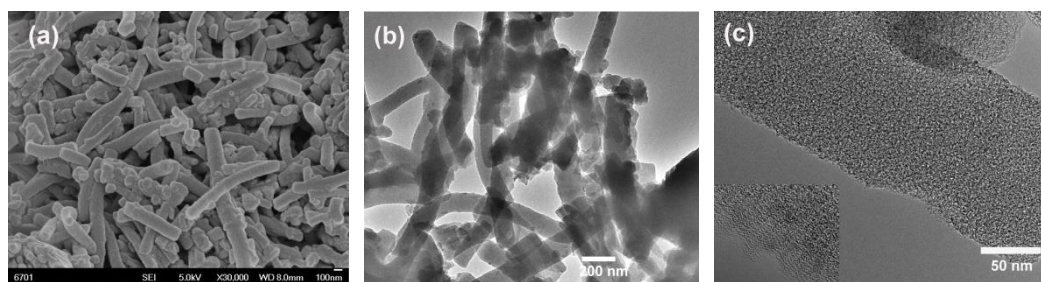


Fig. 5 (a) FESEM and (b-c) HRTEM images of the as-prepared APDC material.

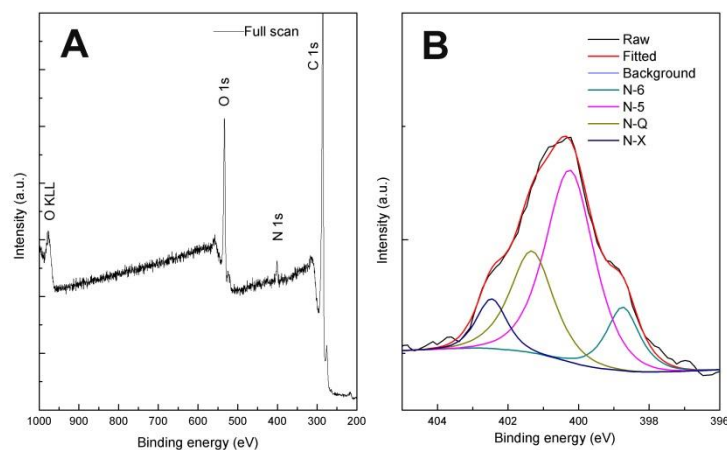


Fig. 6 XPS spectra of APDC powder: panel (A) survey scan and panel (B) N1s core level.

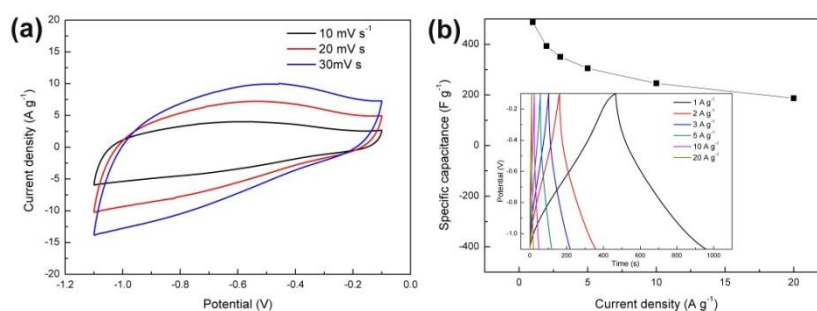


Fig. 7 (a) CV curves at various scan rates and (b) specific capacitance of APDC-based electrode at various current densities. Inset of Fig.7 (b) is corresponding CDC curves.

### 3.3 Electrochemical properties of NiCo-LDH/CNT//APDC ASC device

To further evaluate the practical performance of NiCo-LDH@CNT/NF electrode in full cell configuration, an ASC device with size of  $1 \times 1 \text{ cm}^2$  was assembled by using NiCo-LDH@CNT/NF as positive electrode and APDC/NF as negative electrode. To get  $q^+ = q^-$ , the mass of NiCo-LDH and APDC was set as 8.5 and 17.7 mg, respectively, based on the capacitance values of two electrodes and their corresponding potential windows. Fig. 8a shows the CV curves of the assembled ASC

device at a scan rate of  $10 \text{ mV s}^{-1}$  within different potential windows. As observed, within potential window of 0-1.75 V, the assembled ASC device exhibited quasi-rectangular shaped CV curves coupled with a pair of redox peaks resulted from faradic reactions occurred on NiCo-LDH@CNT/NF and APDC electrodes. As the potential window was extended up to 1.8 V, an undesirable oxygen evolution reaction-induced peak was clearly observed within potential range of 1.75-1.8 V. This suggests that the ASC device can deliver a maximum working voltage of 1.75 V, which was therefore chosen as default voltage value for further investigation. Fig. 8b demonstrates the CV curves of ASC device at scan rate of 5-30  $\text{mV s}^{-1}$ . It was found that, even at high scan rate of  $30 \text{ mV s}^{-1}$ , the CV curve of ASC device still remained the quasi-rectangular shape. No serious distortion was observed, suggesting a quick  $I$ - $V$  response and highly reversible energy storage ability. The discharge curves of the ASC device at various current densities and corresponding cell capacitances are shown in Fig. 8c and d, respectively. Surprisingly, the ASC device can deliver a high cell capacitance of  $210.9 \text{ F g}^{-1}$  at a current density of  $0.5 \text{ A g}^{-1}$ , to best of our knowledge, which is among the highest cell capacitance values reported so far for ASC devices as listed in Table 2. As the discharge current densities increased up to 1, 2, 3, 5, 8 and  $10 \text{ A g}^{-1}$ , high cell capacitances of 190, 175, 159, 134, 120 and  $98 \text{ F g}^{-1}$  were achieved, respectively, implying a good rate capability. The high capacitance value of the asymmetric device is closely related to the high capacitance of positive and negative electrodes.

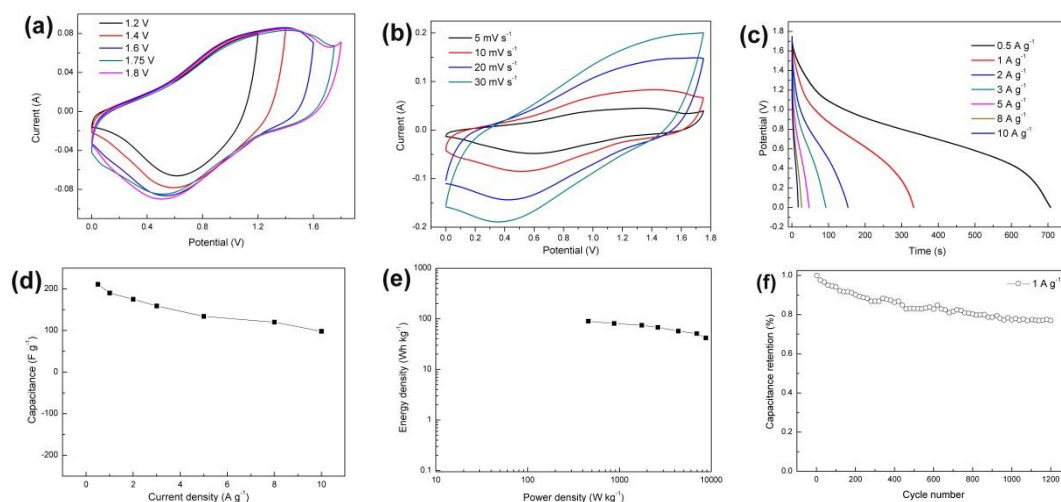


Fig. 8 Electrochemical performance of NiCo-LDH@CNT/NF//APDC/NF ASC device: (a) CV curves at a scan rate of  $10 \text{ mV s}^{-1}$  within different potential windows, (b) CV curves at various sweep rates within potential window of 0-1.75 V, (c) discharge curve and (d) corresponding cell capacitance at various current densities, (e) Ragone plot and (f) cycling stability of the ASC device at  $1 \text{ A g}^{-1}$ .

Energy density and corresponding power density of the ASC device were calculated based on eqns (3-4) and the results are demonstrated as a Ragone plot in Fig. 8e. As demonstrated, the ASC device delivered a maximum energy density of  $89.7 \text{ Wh kg}^{-1}$  at a low power density of  $456.8 \text{ W kg}^{-1}$ . This maximum energy density is much higher than that of traditional AC//AC supercapacitors. The maximum energy density achieved in this study is also higher than those of previous reported ASC devices as listed in Table 2. Encouragingly, as power density increased up to  $8.7 \text{ kW kg}^{-1}$ , the ASC device still can deliver a high energy density of  $41.7 \text{ Wh kg}^{-1}$  which is still higher than that of AC//AC supercapacitor and competitive with that of some ASC devices at low power density ( $<1 \text{ kW kg}^{-1}$ ). More importantly, the high energy density

and power density achieved in this study is realized at mass loading of  $8.5 \text{ mg/cm}^2$ , which well satisfies the prerequisite of high mass loading for commercial applications of supercapacitors. Of course, the cell energy density in this study is calculated based only on the total mass of the NiCo-LDH and APDC. If considering the mass of CNTs and NF on both two electrodes, the packaged cell energy density at power density of  $456.8 \text{ W kg}^{-1}$  will be reduced from 89.7 to  $18.61 \text{ Wh kg}^{-1}$ . Correspondingly, the packaged cell energy density at power density of  $8.7 \text{ W kg}^{-1}$  will be reduced from 41.7 to  $8.65 \text{ Wh kg}^{-1}$ . Since NF current collector has negligible contribution to the packaged cell capacitance or energy density, conversely, it greatly increases the weight of the whole packaged cell. Therefore, for higher packaged cell energy density, lighter current collector would be a good choice in future.

Fig. 8f shows the cycling stability of the ASC device measured at  $1 \text{ A g}^{-1}$ . As demonstrated, the device remained 78% of its original capacitance after 1200 cycles, suggesting an acceptable cycling stability. To further demonstrate its practical application in energy storage and conversion, we assembled two series-connected ASC devices and used to drive commercial electrical components. As demonstrated in Fig. 9a-b and videos S1-3 in supporting information, after charging for 10s by an AA battery, the two series-connected ASC devices can efficiently light a commercial LED indicator (2.0 V, 20 mA) for 10 min and robustly drive a drive a 3V minifan for 4 min, demonstrating its great commercial applications in future.

Table 2 Comparison of the electrochemical performance NiCo-LDH@CNT/NF//APDC/NF ASC

device with those in previous reports.

Asymmetric cell	$C_{\text{positive}}$ ( $F\ g^{-1}$ )	$C_{\text{negative}}$ ( $F\ g^{-1}$ )	$V_{\text{cell}}$ (V)	$C_{\text{cell}}$ ( $F\ g^{-1}$ )	Energy density ( $Wh\ kg^{-1}$ )	Power density ( $kW\ kg^{-1}$ )	$m_{\text{positive}} + m_{\text{negative}}$ ( $mg/cm^2$ )	Ref.
Ni(OH) <sub>2</sub> /CNT//AC	3300	120	1.8	112.5	50.6 (95 $W\ kg^{-1}$ )	1.8 (32.5 $Wh\ kg^{-1}$ )	4.85+20	21
$\beta$ -Ni(OH) <sub>2</sub> /AC	790.3 <sup>c</sup>	---	1.6	105.8	36.2 (100 $W\ kg^{-1}$ )	0.69 (10.5 $Wh\ kg^{-1}$ )	3.8+11.48 <sup>e</sup>	42
Co <sub>3</sub> O <sub>4</sub> /NF//AC	1217	---	1.5	107.3	34 (225)	1.5 (22 $Wh\ kg^{-1}$ )	5+13.25 <sup>e</sup>	43
Ni(OH) <sub>2</sub> /Gra/P-Gra	1735	245	1.6	218.4	77.8 (174.7 $W\ kg^{-1}$ )	15.2 (13.5 $Wh\ kg^{-1}$ )	3+6.8 <sup>e</sup>	44
NiCo <sub>2</sub> O <sub>4</sub> /Gra/HFAC	600	525	1.55	114	48 (230 $W\ kg^{-1}$ )	1.9 (28 $Wh\ kg^{-1}$ )	3.5+5.0	45
GNCC/AC	618	171	1.4	288	19.5	5.6 (7.57 $Wh\ kg^{-1}$ )	10+30	46
GH/MnO <sub>2</sub> /NF	266.8	157.7	2.0	41.7	23.2 (1 $kW\ kg^{-1}$ )	10 (14.9 $Wh\ kg^{-1}$ )	1.0+1.2	47
Gra/MnO <sub>2</sub> //ACN	310	455	1.8	113.5	51.1 (102.2 $W\ kg^{-1}$ )	16.5 (8.2 $Wh\ kg^{-1}$ )	--	48
NiCo <sub>2</sub> S <sub>4</sub> NT/NF/RGO/NF	2398	197	1.55 <sup>e</sup>	4.68 <sup>f</sup>	31.5 (157 $W\ kg^{-1}$ )	2.35 (16.6 $Wh\ kg^{-1}$ )	6+43.5	49
Ni <sub>3</sub> S <sub>2</sub> /CNT//AC	1024	95	1.6	55.8	19.8 (798 $W\ kg^{-1}$ )	6.4 (15.4 $Wh\ kg^{-1}$ )	1.51 (total)	50
NiCo-LDH@CNT/APDC	2046	487	1.75	210.9	89.7 (456.8 $W\ kg^{-1}$ )	8.7 (41.7 $Wh\ kg^{-1}$ )	8.5+17.69	This work

<sup>c</sup>  $C\ g^{-1}$ . <sup>e</sup> Estimated from published graph or data. <sup>f</sup>  $F\ cm^{-2}$ .  $m_{\text{positive}}$  and  $m_{\text{negative}}$  represent the mass loading on positive and negative electrodes, respectively.

P-Gra and NT represent porous graphene and nanotube, respectively.

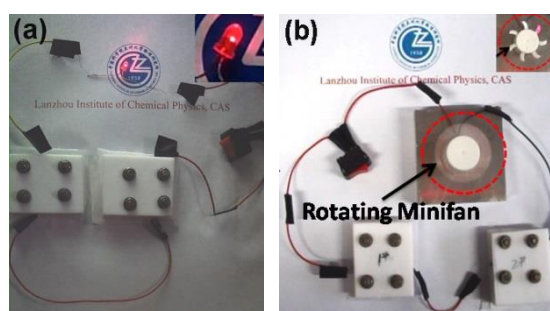


Fig. 9 Camera-captured photographs of (a) LED indicator and (b) minifan driven by two series-connected ASC devices.

#### 4. Conclusions

We have successfully developed 3D core-shell structured NiCo-LDH@CNT/NF positive electrode and APDC-based negative electrode. Results suggest that the integrated CNT/NF composite current collector can greatly increase the mass loading and simultaneously improve the utilization efficiency of electroactive NiCo-LDH. The resulting 3D core-shell structured NiCo LDH@CNT/NF electrode exhibits excellent electrochemical performance at commercial mass loading level. Results also

suggest that activation of carbonized polyaniline precursor is a good strategy to fabricate the N-doped activated carbon for high performance negative electrode. Combined with the high performances of positive and negative electrodes, the assembled NiCo-LDH@CNT/NF//APDC/NF ASC device exhibit a maximum energy density of 89.7 Wh kg<sup>-1</sup> at a power density of 456.8 W kg<sup>-1</sup> and maximum power density of 8.7 kW kg<sup>-1</sup> at an energy density of 41.7 Wh kg<sup>-1</sup>, suggesting its superior supercapacitor performance and demonstrating its great application in energy storage. More importantly, we provide an alternative strategy for constructing high performance ASC device with high cell energy density at commercial mass loading level. In future, the energy density of the ASC device can be further improved if non-aqueous electrolyte is employed.

## ACKNOWLEDGMENT

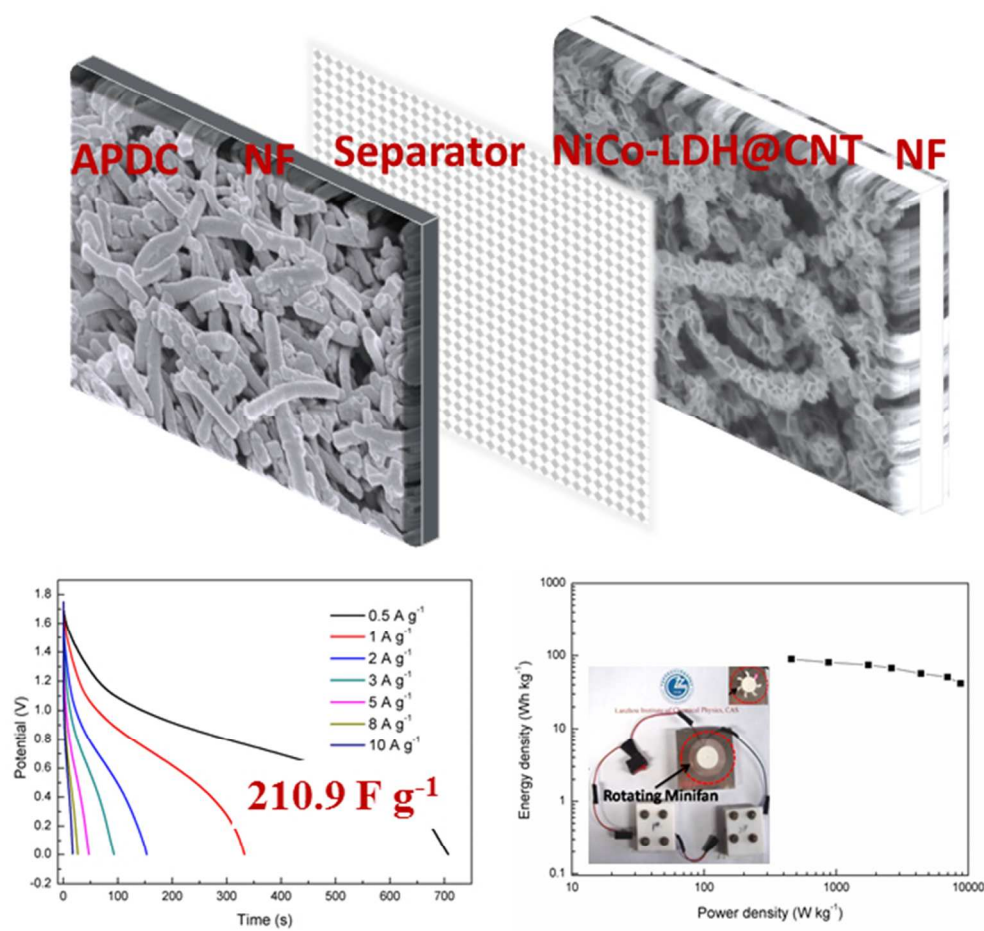
Dr. X. Zhao thanks the financial support offered by the National Natural Science Foundation of China (Grant No. 21306072).

## References:

1. P. Simon and Y. Gogotsi, *Nat. Mater.*, 2008, **7**, 845-854.
2. C. Z. Yuan, H. B. Wu, Y. Xie, X. W. Lou, *Angew. Chem.-Int. Edit.*, 2014, **53**, 1488-1504.
3. C. Shang, S. Dong, S. Wang, D. Xiao, P. Han, X. Wang, L. Gu and G. Cui, *ACS Nano*, 2013, **7**, 5430-5436.
4. H. Chen, L. Hu, M. Chen, Y. Yan and L. Wu, *Adv. Funt. Mater.*, 2014, **24**, 934-942.
5. X. Wang, A. Sumboja, M. Lin, J. Yan and P. S. Lee, *Nanoscale*, 2012, **4**, 7266-7272.
6. Y. Tao, L. Zaijun, L. Ruiyi, N. Qi, K. Hui, N. Yulian and L. Junkang, *J. Mater. Chem.*, 2012, **22**, 23587-23592.
7. L. Huang, D. Chen, Y. Ding, S. Feng, Z. L. Wang and M. Liu, *Nano Lett.*, 2013, **13**, 3135-3139.
8. J.-C. Chen, C.-T. Hsu and C.-C. Hu, *J. Power Sources*, 2014, **253**, 205-213.
9. H. Chen, L. Hu, M. Chen, Y. Yan and L. Wu, *Adv. Funt. Mater.*, 2014, **24**, 934-942.

10. J. Pu, Y. Tong, S. Wang, E. Sheng and Z. Wang, *J. Power Sources*, 2014, **250**, 250-256.
11. L. Xie, Z. Hu, C. Lv, G. Sun, J. Wang, Y. Li, H. He, J. Wang and K. Li, *Electrochimica Acta*, 2012, **78**, 205-211.
12. L.-F. Chen, Z.-H. Huang, H.-W. Liang, H.-L. Gao and S.-H. Yu, *Adv. Funt. Mater.*, 2014, **24**, 5104-5111.
13. S. B. Kulkarni, A. D. Jagadale, V. S. Kumbhar, R. N. Bulakhe, S. S. Joshi and C. D. Lokhande, *Int. J. Hydrogen Energy*, 2013, **38**, 4046-4053.
14. X. Sun, G. Wang, H. Sun, F. Lu, M. Yu and J. Lian, *J. Power Sources*, 2013, **238**, 150-156.
15. J. Yang, C. Yu, X. Fan and J. Qiu, *Adv. Energy Mater.*, 2014, **4**, 1400761.
16. Y. Tao, L. Ruiyi, Z. Li, L. Junkang, W. Guangli and G. Zhiquo, *RSC Adv.*, 2013, **3**, 19416-19422.
17. J. Wang, Y. Song, Z. Li, Q. Liu, J. Zhou, X. Jing, M. Zhang and Z. Jiang, *Energy & Fuels*, 2010, **24**, 6463-6467.
18. L. Zhang, J. Wang, J. Zhu, X. Zhang, K. S. Hui and K. N. Hui, *J. Mater. Chem. A*, 2013, **1**, 9046-9053.
19. M. D. Stoller and R. S. Ruoff, *Energy Environ. Sci.*, 2010, **3**, 1294-1301.
20. Y. Gogotsi and P. Simon, *Science*, 2011, **334**, 917-918.
21. Z. Tang, C.-h. Tang and H. Gong, *Adv. Funt. Mater.*, 2012, **22**, 1272-1278.
22. F. Yang, J. Yao, F. Liu, H. He, M. Zhou, P. Xiao and Y. Zhang, *J. Mater. Chem. A*, 2013, **1**, 594-601.
23. Z. Zhou, X.F. Wu and H. Hou, *Rsc Adv.*, 2014, **4**, 23622-23629.
24. Z. Zhou, X.F. Wu and H. Fong, *Appl. Phys. Lett.*, 2012, **100**, 023115-4.
25. J. Liu, L. Zhang, H. B. Wu, J. Lin, Z. Shen and X. W. Lou, *Energy & Environ. Sci.*, 2014, **7**, 3709-3719.
26. J. Liu, J. Sun and L. Gao, *J. Phys. Chem. C*, 2010, **114**, 19614-19620.
27. J. Liu, M. Chen, L. Zhang, J. Jiang, J. Yan, Y. Huang, J. Lin, H. J. Fan and Z. X. Shen, *Nano Lett.*, 2014, **14**, 7180-7187.
28. S. Dutta, A. Bhaumik and K. C. W. Wu, *Energy Environ. Sci.*, 2014, **7**, 3574-3592.
29. Y. Mao, H. Duan, B. Xu, L. Zhang, Y. Hu, C. Zhao, Z. Wang, L. Chen and Y. Yang, *Energy Environ. Sci.*, 2012, **5**, 7950-7955.
30. L. L. Zhang, X. Zhao, H. Ji, M. D. Stoller, L. Lai, S. Murali, S. McDonnell, B. Cleveger, R. M. Wallace and R. S. Ruoff, *Energy Environ. Sci.*, 2012, **5**, 9618-9625.
31. X. Wang, J. S. Lee, Q. Zhu, J. Liu, Y. Wang and S. Dai, *Chem.Mater.*, 2010, **22**, 2178-2180.
32. H. Zhu, X. Wang, X. Liu and X. Yang, *Adv. Mater.*, 2012, **24**, 6524-6529.
33. L. Qie, W. Chen, H. Xu, X. Xiong, Y. Jiang, F. Zou, X. Hu, Y. Xin, Z. Zhang and Y. Huang, *Energy Environ. Sci.*, 2013, **6**, 2497-2504.
34. X. Li, W. Sun, L. Wang, Y. Qi, T. Guo, X. Zhao and X. Yan, *RSC Adv.*, 2015, **5**, 7976-7985.
35. R. Wang and X. Yan, *Sci. Rep.*, 2014, **4**, 3712.
36. V. Gupta, S. Gupta and N. Miura, *J. Power Sources*, 2008, **175**, 680-685.
37. R. R. Salunkhe, K. Jang, S.-w. Lee, S. Yu and H. Ahn, *J. Mater. Chem.*, 2012, **22**, 21630-21635.
38. L. Zhang, X. Zhang, L. Shen, B. Gao, L. Hao, X. Lu, F. Zhang, B. Ding and C. Yuan, *J. Power Sources*, 2012, **199**, 395-401.
39. Y. Tan, C. Xu, G. Chen, Z. Liu, M. Ma, Q. Xie, N. Zheng and S. Yao, *ACS Appl. Mater.*

- Interfaces*, 2013, **5**, 2241-2248.
40. D.-W. Wang, F. Li, L.-C. Yin, X. Lu, Z.-G. Chen, I. R. Gentle, G. Q. Lu and H.-M. Cheng, *Chem. Eur. J.*, 2012, **18**, 5345-5351.
41. X. Qing, Y. Cao, J. Wang, J. Chen and Y. Lu, *RSC Adv.*, 2014, **4**, 55971-55979.
42. J. Huang, P. Xu, D. Cao, X. Zhou, S. Yang, Y. Li and G. Wang, *J. Power Sources*, 2014, **246**, 371-376.
43. X. Zhang, Y. Zhao and C. Xu, *Nanoscale*, 2014, **6**, 3638-3646.
44. J. Yan, Z. Fan, W. Sun, G. Ning, T. Wei, Q. Zhang, R. Zhang, L. Zhi and F. Wei, *Adv. Funt. Mater.*, 2012, **22**, 2632-2641.
45. Z. Li, Z. Xu, H. Wang, J. Ding, B. Zahiri, C. M. B. Holt, X. Tan and D. Mitlin, *Energy Environ. Sci.*, 2014, **7**, 1708-1718.
46. Z. Wen, X. Wang, S. Mao, Z. Bo, H. Kim, S. Cui, G. Lu, X. Feng and J. Chen, *Adv. Mater.*, 2012, **24**, 5610-5616.
47. H. Gao, F. Xiao, C. B. Ching and H. Duan, *ACS Appl. Mater. Interfaces*, 2012, **4**, 2801-2810.
48. Z. Fan, J. Yan, T. Wei, L. Zhi, G. Ning, T. Li and F. Wei, *Adv. Funt. Mater.*, 2011, **21**, 2366-2375.
49. H. Chen, J. Jiang, L. Zhang, D. Xia, Y. Zhao, D. Guo, T. Qi and H. Wan, *J. Power Sources*, 2014, **254**, 249-257.
50. C.-S. Dai, P.-Y. Chien, J.-Y. Lin, S.-W. Chou, W.-K. Wu, P.-H. Li, K.-Y. Wu and T.-W. Lin, *ACS Appl. Mater. Interfaces*, 2013, **5**, 12168-12174.



An asymmetric supercapacitor device with energy density of 89.7 Wh kg<sup>-1</sup> at commercial level mass loading was successfully fabricated.  
178x171mm (96 x 96 DPI)